Bulletin of Mathematical Biology (2008) 70: 1192–1215
DOI 10.1007/s11538-008-9296-3

ORIGINAL ARTICLE

An Integrative Computational Model of Multiciliary Beating

Xingzhou Yang[a,*], Robert H. Dillon[b], Lisa J. Fauci[c]

[a] *Center for Computational Science, Tulane University, New Orleans, LA 70118, USA*
[b] *Department of Mathematics, Washington State University, Pullman, WA 99163, USA*
[c] *Department of Mathematics, Tulane University, New Orleans, LA 70118, USA*

Received: 11 July 2007 / Accepted: 20 November 2007 / Published online: 31 January 2008

Abstract The coordinated beating of motile cilia is responsible for ovum transport in the oviduct, transport of mucus in the respiratory tract, and is the basis of motility in many single-celled organisms. The beating of a single motile cilium is achieved by the ATP-driven activation cycles of thousands of dynein molecular motors that cause neighboring microtubule doublets within the ciliary axoneme to slide relative to each other. The precise nature of the spatial and temporal coordination of these individual motors is still not completely understood. The emergent geometry and dynamics of ciliary beating is a consequence of the coupling of these internal force-generating motors, the passive elastic properties of the axonemal structure, and the external viscous, incompressible fluid. Here, we extend our integrative model of a single cilium that couples internal force generation with the surrounding fluid to the investigation of multiciliary interaction. This computational model allows us to predict the geometry of beating, along with the detailed description of the time-dependent flow field both near and away from the cilia. We show that synchrony and metachrony can, indeed, arise from hydrodynamic coupling. We also investigate the effects of viscosity and neighboring cilia on ciliary beat frequency. Moreover, since we have precise flow information, we also measure the dependence of the total flow pumped per cilium per beat upon parameters such as viscosity and ciliary spacing.

Keywords Multiciliary beating · Synchrony · Metachrony · Beat frequency · Viscosity changes · Interciliary spacing · Immersed boundary method

1. Introduction

Cilia are microscopic, hair-like organelles projecting from a cell's surface. In the human body, cilia have been identified on almost all cells, including embryonic, kidney, and brain cells (Marshall and Nonaka, 2006). Afzelius (2004) reported that there are at least eight categories of cilia or cilia-derived organelles with lengths ranging from

---

*Corresponding author.

E-mail addresses: xingzhou.yang@tulane.edu (Xingzhou Yang), dillon@math.wsu.edu (Robert H. Dillon), fauci@tulane.edu (Lisa J. Fauci).

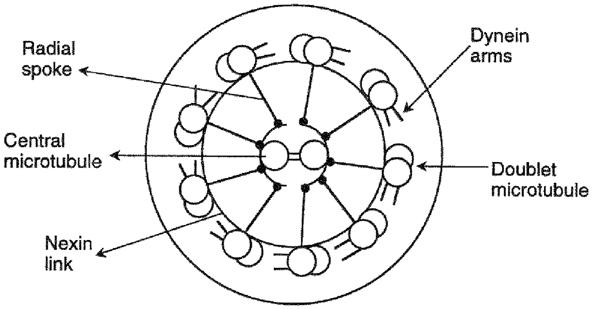

Fig. 1 Schematic of an axoneme cross-section, depicting 9 microtubule doublets and the central pair of two microtubules. Also depicted are the dynein motors, the nexin links, and the radial spokes.

about 2 μm to 50 μm. Motile cilia are central to ovum transport in the oviduct, transport of mucus across respiratory epithelia, and cerebrospinal fluid movement in the brain (Talbot et al., 1999; Afzelius, 2004; Pan et al., 2005; Davenport and Yoder, 2005; Fauci and Dillon, 2006). Other cilia serve important sensory functions, and play a key role in the development and homeostasis of cell proliferation (Avidor-Reiss et al., 2004; Snell et al., 2004). Ciliary defects lead to a surprisingly wide range of clinical problems from polycystic kidney disease (PKD) to syndromes associated with obesity, hypertension, diabetes rhinitis, sinusitis, bronchiectasis, and retinitis pigmentosa (Afzelius, 1976, 2004, Eley et al., 2005; Pan et al., 2005; Davenport and Yoder, 2005; Fliegauf and Omran, 2006). For a recent review of cilia in human development and disease, see Vogel (2005).

A cilium consists of a basal body and an axonemal core covered by a plasma membrane. The axoneme in a motile "9 + 2" cilium has two central microtubule singlets surrounded by nine microtubule doublets. A schematic of a cross-section depicting this "9 + 2" axonemal structure is shown in Fig. 1. The nine outer doublets are connected by radial spokes to a sheath surrounding the central pair. Other protein structures such as nexin serve as structural links supporting the axoneme. Thousands of dynein molecular motors are distributed along the length and circumference of the axoneme, each attached permanently at one end to an outer doublet, and able to attach and detach dynamically to the neighboring doublet. The beating of the cilium is achieved by ATP-driven dynein activation cycles that cause neighboring microtubule doublets to slide relative to each other (Witman, 1990; Murase, 1992). The precise nature of the spatial and temporal control mechanisms regulating the ciliary beat is still unknown (Brokaw, 2001). Considerable interest has been focused on understanding how the local force production of the dynein motors is translated into the controlled, regular beating of the single cilium, as well as the coordinated beating of multiciliary arrays. When neighboring cilia in a multiciliary array beat with regular phase differences between them, coherent traveling waves propagate on the surface of the array. These metachronal waves are used by paramecium to swim, and by respiratory cilia to propel mucus.

The external, viscous fluid environment in which the cilium beats is an integral component of this complex, coupled mechanical system. In the past 50 years, there have been many successful mathematical models that capture various aspects of the fluid dynamics of ciliary and flagellar beating. In their classical resistive force theory, Gray and Hancock (1955) describe the cilium by a series of cylinders and assume that the local force on each cylinder is proportional to the local velocity. Central to this approach is the use of estimated resistance coefficients. Models for ciliary and flagellar motion based on a generalized resistive force theory have been developed and explored by several researchers (Brokaw, 1972; Hines and Blum, 1978, 1979). A comprehensive review of this class of mathematical models is presented by Murase (1992). Lighthill (1967) improved this theory by incorporating slender body approximations since the diameter of a cilium is much smaller than its length. More detailed hydrodynamic analysis, such as refined slender body theory and boundary element methods has produced excellent simulations of both two- and three-dimensional flagellar propulsion in an infinite fluid domain or in a domain with a fixed wall (Dresdner et al., 1980; Higdon, 1979a, 1979b; Phan-Thien et al., 1987). In all of these fluid dynamical models, the shape and the kinematics of the ciliary or flagellar beat was taken as given. Of course, the actual geometry of a beating cilium is an emergent property of the coupled system consisting of the internal force generating mechanisms, the passive elastic structure, and the external fluid dynamics. Several models of ciliary beating have been developed that include both internal bend-generating mechanics and fluid dynamics. The models of Gueron et al. (1997), Gueron and Levit-Gurevich (1998, 1999) use digitized data from a beating paramecium cilium to back out the parameters of an internal force engine that depends upon the ciliary geometry. The force due to this engine is then coupled to hydrodynamics using a revised slender body theory. Velocities and evolving beat geometries of a ciliary array are computed. Realistic beat patterns emerge, and ciliary synchrony and metachrony are shown to be a result of hydrodynamic coupling. An extension of this model that includes a representation of internal force generation for three-dimensionalcilia is presented in Gueron and Levit-Gurevich (2001).

Camalet and Jülicher (2000) presented an elastic rod model of a cilium whose dynamics are driven by internal stresses that result from tracking internal, active elements. A simple hydrodynamic model using frictional coefficients was employed (Wiggins and Goldstein, 1998; Wiggins et al., 1998), and small deformations of the filaments were assumed. Recently, this model has been extended by Guirao and Joanny (2007) to investigate the emergence of metachronal waves in an array of cilia. The simplified hydrodynamics uses a coarse-grained approach where the effect of the cilia on the flow is replaced by an effective force, and assumes that neighboring cilia are far away from each other. A mean field approximation is used to compute a uniform, scalar velocity due to ciliary beating. Another model of multiciliary interaction that does include a more detailed treatment of hydrodynamics is due to Vilfan and Jülicher (2006). Here, a minimal model represents the cilium by a small sphere at the center of mass. The flow field generated by the periodic motion of this sphere is calculated using image Stokeslet solutions to the governing Stokes equations in the presence of a planar boundary. Here, a state diagram is presented indicating synchronized states between two cilia as a function of their distance.

In this paper, we use as a starting point our model of ciliary beating that incorporates discrete representations of dynein arms, the passive elastic structure of the axoneme including the doublets, and nexin links presented in Dillon and Fauci (2000), Dillon et al. (2003). Dynein activation is governed by a simple curvature control mechanism (Brokaw, 1972). This model, based upon the immersed boundary method (Peskin, 2002), couples the internal forces generated by the dynein motors with the external, viscous fluid mechanics. Within the immersed boundary framework, the forces due to each cilium are communicated to the fluid region in which it sits. As each additional cilium in the same fluid domain adds to the external force field, the fluid dynamic interactions of multiple cilia is readily achieved with little additional computational cost.

We emphasize that the model presented here does not take the ciliary beat form as given, nor utilize digitized data to derive forces, but constructs the cilium itself out of mechanical elements. The properties of these elements can be adapted to test internal mechanisms of force generation. Since the resulting forces are fully coupled to the surrounding fluid, one may directly evaluate the affects of the viscous environment on the emergent beat characteristics of individual cilia, as well as ciliary interactions. In Section 2, we present the simple axonemal representation of the cilia, the mathematical framework describing the coupled fluid-structure system, and the computational algorithm used to solve this system. We present numerical results that demonstrate how synchrony and metachrony evolve between neighboring cilia arising from hydrodynamic interactions. We also examine the effects of viscosity and ciliary spacing on beat frequency and fluid transport. A discussion of the model, the numerical experiments, and future model enhancements is also presented.

2. Mathematical model

The bending of the three-dimensional axoneme is caused by sliding between pairs of outer doublets. Active sliding is due to the unidirectional ATP-induced force generation of the dynein power stroke. Backward, passive sliding is due to the active sliding of other pairs of doublets within the axoneme. Here we present a two-dimensional model of a simplified axoneme that is comprised of only two microtubules. A schematic for this model cilium is shown in Fig. 2. Each microtubule consists of a pair of parallel microtubule filaments built out of a series of links that are also supported by diagonal cross-links. These links give the microtubules structural rigidity. The dyneins and nexin links are represented in the model as forces which act upon the microtubule filaments. We assume that the filaments are highly resistant to stretching and compression but not to bending. In the ciliary model, we include two sets of dyneins that share the same space between the two microtubules. We activate one set (E) during the effective stroke and a second set (R) during the recovery stroke. The effective stroke (E) dyneins are shown in Fig. 2 (left), and the recovery stroke (R) dyneins are shown in Fig. 2 (right). During the effective stroke, the (E) dyneins contract. These forces pull the microtubule on the right upward, and push the microtubule on the left downward. Since the microtubules are tethered to fixed spatial points at the cell wall at the microtubule base, the contraction of dyneins results in bending toward the right. The (E) dyneins are permanently attached to the microtubule on the left, but transiently attached to a nearby site on the microtubule on the right. This dynein attachment and connectivity is a dynamic process that must be determined during the computation. During the recovery stroke, the (R) dyneins contract, producing a bending toward the left. Note that in the true three-dimensional axoneme, the dyneins between adjacent pairs of doublet microtubules produce active sliding forces in only one direction. A coordinated ciliary beat requires an activation of dyneins on one side of the circular cross-sections of the axoneme, followed by an activation of the dyneins on the other side. Thus, our model can be viewed as a model of the entire axoneme in which each of the model microtubules

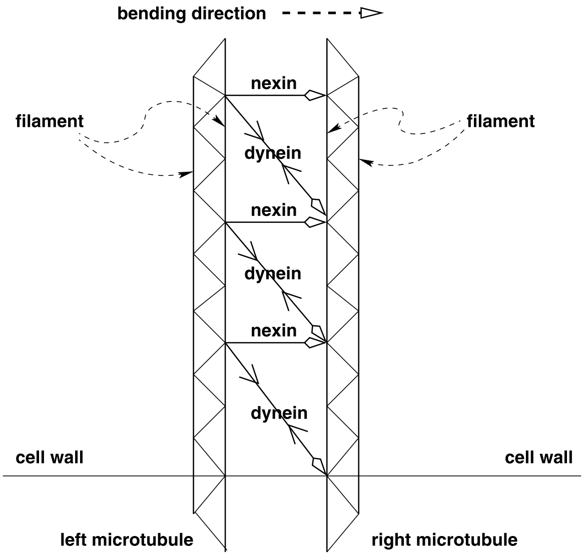

(a) bending from left to right

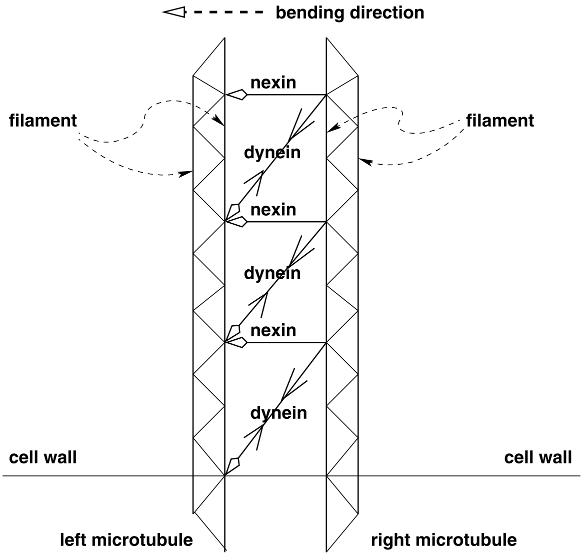

(b) bending from right to left

Fig. 2 Schematic of model ciliary axoneme during (E) effective stroke and (R) recovery stroke. Each microtubule is built from two parallel microtubule filaments. Here we assume that the effective stroke will bend toward the right. The dynein links are depicted as diagonal links with open arrows pointing downward from their permanent attachment points (on the left microtubule for (E) dyneins and on the right microtubule for (R) dyneins). The horizontal links with open arrows are the nexin structural links of the model axoneme. The contraction of the dynein links (depicted by arrows) causes local sliding between the microtubules, and this sliding is converted to bending.

represents one half of the $9+2$ axoneme. Similarly, the (E) and (R) dyneins represent the dyneins on each half of the axoneme.

The formulation of our model is based upon the immersed boundary method (Peskin, 1977, 2002). This method provides a framework for coupling elastic dynamics of flexible boundaries with a surrounding viscous, incompressible fluid. These elastic objects are accounted for by suitable contributions to a force term in the fluid-dynamics equations. The force of each object on the fluid is a Dirac delta-function layer of force supported only by the region of fluid that coincides with material points of the object. Once these forces on the fluid are accounted for, one can solve the fluid-dynamics equations efficiently on a finite difference or finite element grid.

The fluid is regarded as viscous and incompressible, and the filaments that comprise the microtubules of the axoneme as elastic boundaries immersed in this fluid. We assume that the flow is governed by the Navier–Stokes equations:

$$\rho\left[\frac{\partial \mathbf{u}}{\partial t} + \mathbf{u}\cdot\nabla\mathbf{u}\right] = -\nabla p + \mu\Delta\mathbf{u} + \mathbf{F}(\mathbf{x},t), \tag{1}$$

$$\nabla\cdot\mathbf{u} = 0, \tag{2}$$

where ρ is the fluid density, μ is the fluid viscosity, t is time, and $\mathbf{u}$ is the fluid velocity, p denotes the pressure, and $\mathbf{F}$ is the force density which is exerted on the fluid by the axoneme and cell wall. The force density $\mathbf{F}$ in Eq. (1)

$$\mathbf{F} = \mathbf{F}_{\mathrm{M}} + \mathbf{F}_{\mathrm{N}} + \mathbf{F}_{\mathrm{D}} + \mathbf{F}_{\mathrm{C}} + \mathbf{F}_{\mathrm{T}} \tag{3}$$

includes contributions arising from the deformation of the elastic structure of the microtubules $\mathbf{F}_{\mathrm{M}}$, elongation of the nexin links $\mathbf{F}_{\mathrm{N}}$, contraction of the dynein links $\mathbf{F}_{\mathrm{D}}$ as well as tethering forces that prevent movement of the cell wall $\mathbf{F}_{\mathrm{C}}$ and the base of the axoneme $\mathbf{F}_{\mathrm{T}}$.

Let $\mathbf{X}^{k,ia}(s,t)$ represent the "kth" microtubule filament ($k = 1, 4$) of the "iath" axoneme or cilium. Here s is a Lagrangian parameter, such as arclength in an unstressed configuration, measured along each filament. The mass of these neutrally-buoyant filaments is attributed to the mass of the fluid in which they sit, and thus the passive and elastic forces at material points of the filaments are transmitted directly to the fluid. The force densities $\mathbf{F}_X$, $X = \mathrm{M, N, D, T}$ and $\mathbf{F}_{\mathrm{C}}$ in Eq. (3) are, therefore:

$$\mathbf{F}_X(\mathbf{x},t) = \sum_{k,ia}\int_{\text{filaments}} \mathbf{f}_X^{k,ia}(s,t)\,\delta\big(\mathbf{x} - \mathbf{X}^{k,ia}(s,t)\big)\,ds, \tag{4}$$

$$\mathbf{F}_{\mathrm{C}}(\mathbf{x},t) = \int_{\text{Cell wall}} \mathbf{f}_{\mathrm{C}}(s,t)\,\delta\big(\mathbf{x} - \mathbf{X}_{\mathrm{C}}(s,t)\big)\,ds, \tag{5}$$

where δ is the two-dimensional Dirac delta-function, $\mathbf{f}_X^{k,ia}$ is the boundary force per unit length along the kth microtubule filament of the iath axoneme and $\mathbf{f}_{\mathrm{C}}(s,t)$ is the force per unit length along the cell wall whose configuration is given by $\mathbf{X}_{\mathrm{C}}(s,t)$.

Each of the forces $\mathbf{f}_X^{k,ia}$ and $\mathbf{f}_{\mathrm{C}}(s,t)$ are derived from spring forces. For instance, the passive elastic forces $\mathbf{f}_{\mathrm{M}}^{k,ia}$ due to the structural springs of the microtubules contain contributions of the form:

$$-S_f\big(\|\mathbf{X}_{i+1}^{k,ia} - \mathbf{X}_i^{k,ia}\| - \Delta S_f\big)\frac{\mathbf{X}_i^{k,ia} - \mathbf{X}_{i+1}^{k,ia}}{\|\mathbf{X}_i^{k,ia} - \mathbf{X}_{i+1}^{k,ia}\|}. \tag{6}$$

Here S_f is a spring constant that is chosen to reflect the material properties of the microtubules, and $X_i^{k,ia}$ represents the ith discrete point of the microtubule filament ($i = 1, np$, where np is the total number of discrete points on a microtubule filament). Note that these forces are due to springs with resting length ΔS_f connecting adjacent points of the filaments. Other forces due to cross-connections within the microtubules depicted in Fig. 2 are also included.

The dynamic forces arising from the activation of individual dyneins are of the form:

$$\mathbf{f}_i^L = -S_{\text{dyn}}\big(\mathbf{X}_i^L - \mathbf{X}_{j(i)-M}^R\big), \tag{7}$$

Note that this (E) dynein force may be thought of as arising from a spring with resting length zero that connects a point X_i^L on the left microtubule to a point $X_{j(i)-M}^R$ on the right microtubule. The index $j(i)$ is chosen to minimize the distance $\|\mathbf{X}_i^L - \mathbf{X}_{j(i)}^R\|$. Hence, these are dynamic springs that change connectivity during the course of the computation. The offset M and the stiffness constant S_{dyn} are numerical parameters that may be chosen to reflect the force strength of each individual dynein. In the simulations presented in this manuscript, the offset parameter was chosen to be $M = 2$. The forces due to nexin links are also modeled as dynamic springs between the microtubules that act to keep them a fixed distance apart. Finally, to keep the base of each cilium as well as the cell wall fixed in space, tethering forces due to strong springs connect these immersed boundary points to prescribed spatial positions (see Dillon and Fauci, 2000).

These forces defined on the microtubules are communicated to the fluid domain using discrete versions of Eqs. (4)–(5). In the computations presented here, we follow Peskin (1977) and choose the discrete delta-function $\delta_h(\mathbf{x}) = d(x)d(y)$ where h is the mesh width of the fluid grid:

$$d(r) = \begin{cases} \frac{1}{4h}\left(1 + \cos\frac{\pi r}{2h}\right), & |r| < 2h, \\ 0, & |r| \geq 2h. \end{cases} \tag{8}$$

Our coupled fluid-axoneme system is closed by requiring that the velocity of the microtubules and cell wall must be equal to the local fluid velocity at each point.

$$\frac{\partial \mathbf{X}(s,t)}{\partial t} = \mathbf{u}\big(\mathbf{X}(s,t),t\big) = \int \mathbf{u}(\mathbf{x},t)\delta\big(\mathbf{x} - \mathbf{X}(s,t)\big)\,d\mathbf{x} \tag{9}$$

where $\mathbf{X} = \mathbf{X}^{k,ia}$ or $\mathbf{X}_{\text{C}}$ and the integration is over the entire fluid domain.

Within this modeling framework, at each time step, we have detailed geometric information available for each cilium such as the curvature of the microtubules, the stretching of nexin links, and the amount of shear or sliding between the microtubules. For the model cilia presented here, we choose a curvature-control algorithm motivated by Brokaw (1972). The discrete dyneins in each cilia obey the following rules of activation: In the effective mode, we activate all (E) dyneins. The end of the effective stroke is reached when the right microtubule has slid SD attachment units with respect to the left microtubule at the axonemal tip. This condition is reached when $np - j(np) = SD$. In the recovery mode, (E) dyneins are inactive. The (R) dyneins are activated in a traveling wave from base to tip by means of a curvature-control algorithm in the following manner. At time level t^n, we calculate the index p^n that corresponds to the point of maximum curvature on the unfolding ciliary axoneme. All (R) dyneins at time t^n with indices less than p^n

are then activated and all (R) dyneins with indices greater than p^n are inactive. This algorithm is described in more detail in Dillon and Fauci (2000). The end of the recovery stroke is determined in a way analogous to the end of the effective stroke. In this case, the axoneme switches from recovery mode to effective mode when the left microtubule has slid SD units distally with respect to the tip of the right microtubule.

The numerical algorithm may be summarized as follows: At the end of a time step n we have the fluid velocity field $\mathbf{u}^n$ on our finite difference grid, and the configuration of the immersed boundary points comprising the filaments of the microtubules $(\mathbf{X}_i^{k,ia})^n$ and the cell wall $(\mathbf{X}_c)^n$. To advance to the next step we:

1. Use the geometric switch algorithm to determine whether each cilium is in effective or recovery mode.
2. Use geometric information to determine activation and connectivity properties of discrete dyneins for each individual cilium.
3. Calculate force densities along microtubules of each cilium and the cell wall.
4. Use discrete delta-functions to spread force densities to the fluid domain.
5. Solve the Navier–Stokes equations for $\mathbf{u}^{n+1}$.
6. Interpolate grid velocities to immersed boundary points using the discrete delta-functions, and update their positions to arrive at $(\mathbf{X}_i^{k,ia})^{n+1}$ and $(\mathbf{X}_c)^{n+1}$.

Note that the dynein activation dynamics are determined separately for each individual cilium. For instance, within a simulation, there may be some cilia in the power stroke, and some in the recovery stroke. However, each of the cilia interact through their coupling with the surrounding viscous, incompressible fluid. For the solution of the Navier–Stokes equations, we use an FFT-based solver. Since additional cilia interacting in the same fluid domain act as additional contributions to the force density term in the Navier–Stokes equations, the cost of computing forces due to N cilia is just $O(N)$.

3. Numerical results

We present an illustrative simulation of two adjacent cilia beating in Fig. 3. This series of snapshots show the evolution of the ciliary beat, the fluid velocity field, and the evolution of a cloud of fluid markers within the fluid domain. Each cilium is composed of two microtubules, which can be seen in the figure. Note that the tip of the microtubule on the inner part of the bend in each cilium is extended, showing that sliding that has occurred between the microtubules. The individual dynein "springs" that drive this sliding are not depicted in this figure, but occupy the space between the two microtubules, as do the nexin "springs" (also not shown).

These two cilia are identical in the sense that they have the same material properties, the same initial configuration of dynein activation, same geometric switch between the power and recovery strokes, and same curvature controlled algorithm that determines the evolution of the recovery stroke. However, we see from Fig. 3 that their beat patterns are not identical—their evolving shape is determined by the fluid dynamics. Here the periodic domain has dimensions of 40 μm × 40 μm, and is discretized using a 256 × 256 finite difference grid. The length of the cilium is approximately 14 μm, and each filament of a ciliary microtubule is described by 120 discrete immersed boundary points. Either an (E) or (R) dynein is associated to each of the discrete points of the inner microtuble filaments,

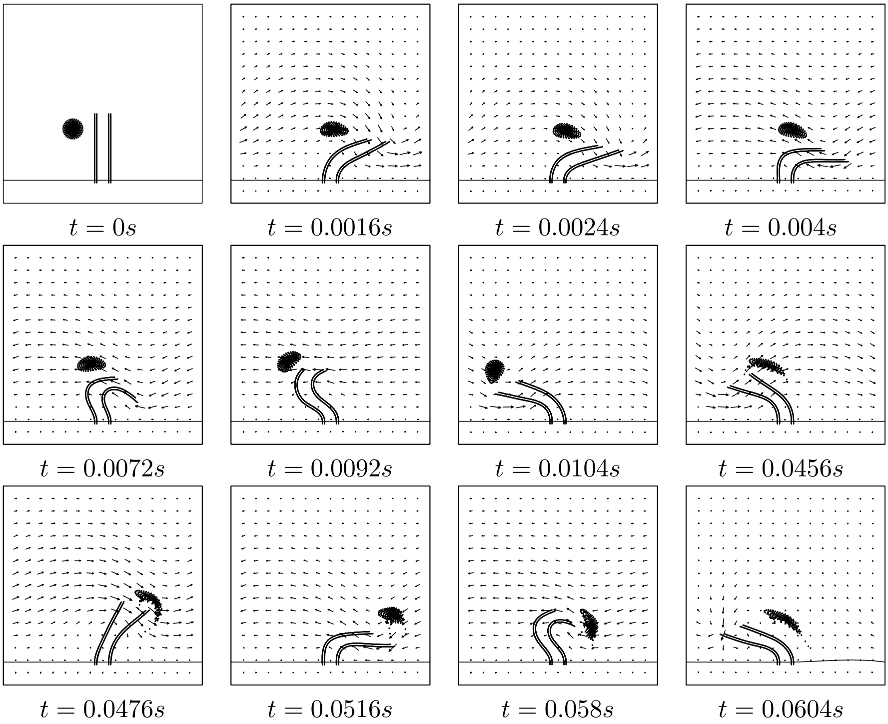

Fig. 3 Snapshots of velocity fields of 2 cilia at different times. A patch of neutrally buoyant fluid markers is tracked as it is advected by the flow. The beat frequency is 59 Hz.

except at a short region at the base where no sliding is allowed. Hence, each cilium has at least 100 (E) dyneins and 100 (R) dyneins. Other governing material parameters are identical to those described in Dillon and Fauci (2000).

In this model, it is important to use material parameters for microtubules and dynein springs that reflect the properties of true cilia. Since the coupled fluid-cilia system is described using the 2D equations of fluid dynamics, we must take care in translating the two-dimensional parameters and units to their three-dimensional counterparts. For instance, the amount of force generated by a dynein link at the moment it is activated, in our model, is about 2.5×10^{-2} dynes per unit length. We choose our length scale to be on the order of the intermicrotubule distance in our model, which is a few grid spacings, $dz = 1.5 \times 10^{-5}$ cm. This gives us a dynein force of about 4 pN, which is in the range of 1–5 pN reported by Howard (2001), Lindemann (2003). In order to estimate the bend modulus or flexural rigidity of our elastic model axoneme, we follow the procedure of Lim and Peskin (2004). We initialize the structure in the form of an arc with curvature K, and compute the total energy in the springs that comprise the mechanical model. Using the relation $E = \frac{1}{2}AK^2L$, where A is the bend modulus, L is the ciliary length, we compute in our two-dimensional case, $A = 0.6 \times 10^{-8}$ dynes cm. For comparison with the three-dimensional axoneme, we need to multiply by a length scale to achieve a bend modulus with units dynes cm^2. Again, using a length scale on the order of the microtubule distance, we arrive at a bend modulus of about 10^{-21} N m^2. Note that the bend modulus measured for sea urchin sperm lies in the range 0.6–12 × 10^{-21} N m^2 (Howard, 2001; Ishijima and Hiramoto, 1994). Of course, translating each of these parameters (dynein force and bend modulus) from its two-dimensional units to its three-dimensional counterpart made use of a scale factor, which though plausible, may be suspect. We remark that even without choosing a scale factor, we may assert that the ratio of axoneme bend modulus to dynein force strength in our model fits well within the range of ratios exhibited by biological cilia and flagella.

The resulting beat frequency that emerges as a consequence of the coupling of external fluid mechanics with the internal dynamics of our model cilia in Fig. 3 is about 59 Hz. As in all of the simulations presented in this manuscript, this reflects dynein motor forces at the high end of about 4 pN. It is unlikely that this large force per dynein is achieved during dynamic sliding. We remark that when we cut the stiffness constants for the dynein motor springs in half, the resulting beat frequency reduces to about 33 Hz. Although these are faster than beat frequencies reported for respiratory cilia (10–13 Hz) (Chilvers and O'Callaghan, 2000), they are in line with the beat frequencies of about 60 Hz measured for Chlamydomonas flagella, which undergo a ciliary beat (Brokaw and Luck, 1983).

3.1. Synchrony and metachrony

It has long been established that hydrodynamic forces are central to the coordination of motile structures at the microscopic level. Randomly distributed flagella of the peritrichously flagellated bacteria such as *Escherichia coli* form a coherent bundle behind the cell during forward swimming (Darnton et al., 2004). This bundling is due to hydrodynamic interactions (Flores et al., 2005; Powers, 2001; Kim et al., 2003). Note that the prokaryotic bacterial flagella are fundamentally different from eucaryotic cilia and flagella as they are driven solely by a rotary motor at their base.

Hydrodynamic entrainment of spermatozoa was noted by Gray (1928). Nearby swimming sperm tend to beat in phase (Taylor, 1951). This phase-locking phenomenon of flagellar swimming was demonstrated using computational studies in Fauci and McDonald (1994). Hydrodynamic coupling has also been implicated in the generation of ciliary metachronal waves, whereby neighboring cilia beat in synchrony, but a continuous phase difference results in the ciliary tips forming a traveling wave (Childress, 1981). This coordinated beating allows respiratory cilia to clear mucus from the lungs, and single-celled organisms to swim. Recently, hydrodynamic feedback was shown to direct planar polarity of cilia in the developing *Xenopus* embryo (Mitchell et al., 2007).

In previous studies, Gueron et al. (1997), Gueron and Levit-Gurevich (1998) used their model to obtain self-synchronization between two adjacent cilia. Fast self-synchronization is reported with intercilia spacing in the range of 0.3 to 1.5 cilium lengths in Gueron and Levit-Gurevich (1998). In addition, metachrony was shown to develop in linear arrays of cilia.

Our model also shows that hydrodynamic forces cause the rapid synchronization of beating for closely spaced cilia. Fig. 4 shows snapshots of a simulation where two cilia, initially at different phases of their power stroke, begin beating in a fluid at rest. The ciliary beats quickly synchronize, and settle into a regular beat frequency of about 64 Hz. The snapshots are not equally spaced in time, but show positions during the first couple of beat periods, and later positions during the sixth beat period.

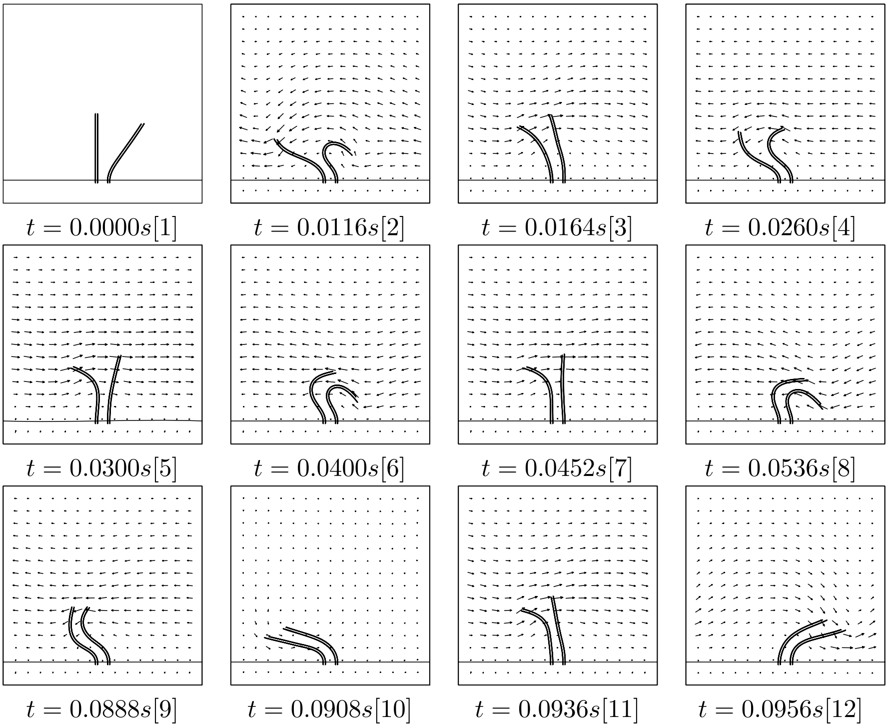

$t = 0.0000s[1]$ $t = 0.0116s[2]$ $t = 0.0164s[3]$ $t = 0.0260s[4]$

$t = 0.0300s[5]$ $t = 0.0400s[6]$ $t = 0.0452s[7]$ $t = 0.0536s[8]$

$t = 0.0888s[9]$ $t = 0.0908s[10]$ $t = 0.0936s[11]$ $t = 0.0956s[12]$

Fig. 4 Snapshots of synchronization of two cilia initially at different phases of the effective stroke. The numbers in the bracket correspond to the denoted times on the synchronization graph shown in Fig. 5.

Motivated by Gheber and Priel (1989), we define the following function in order to quantify the synchronization of neighboring cilia:

$$syn(t) = \sqrt{\frac{1}{np}\sum_{k=1}^{np}\big(d_k(t) - \bar{d}(t)\big)^2},$$

where

$$d_k(t) = \frac{\|\boldsymbol{X}_{\text{left}}(k,t) - \boldsymbol{X}_{\text{right}}(k,t)\|}{\text{ciliary length}}, \quad \text{for } k = 1, 2, \ldots, np,$$

and

$$\bar{d}(t) = \frac{1}{np}\sum_{k=1}^{np} d_k(t).$$

$\boldsymbol{X}_{\text{left}}(k,t)$ or $\boldsymbol{X}_{\text{right}}(k,t)$ $(k = 1, 2, \ldots, np)$ are the coordinates of the immersed points on a selected microtubule filament of the left or right cilium at time t. We choose the corresponding filaments on the cilia. If the two cilia had identical beat pattern, $syn(t)$

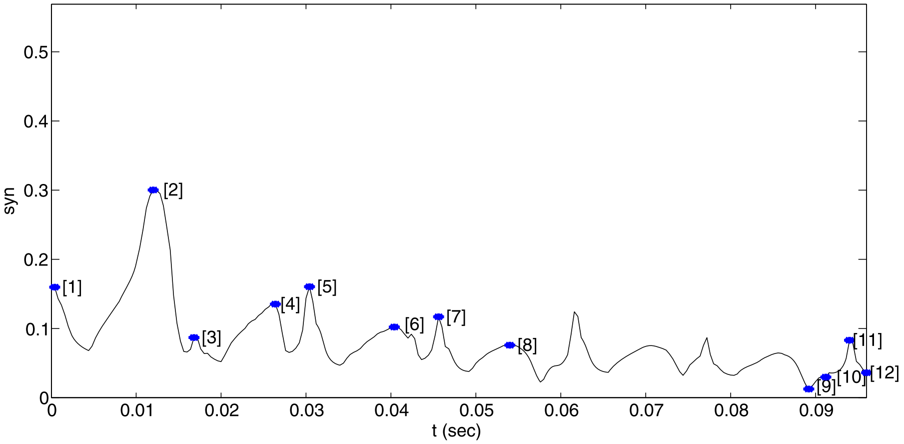

Fig. 5 Synchronization measurement for the simulation depicted in Fig. 4. The numbers shown on the graph correspond to the geometry of the two cilia shown in the indicated frame in Fig. 4.

would be identically zero. The smaller the function value $syn(t)$ is, the larger the degree of synchronization. Fig. 5 shows the evolution of the synchronization as a function of time. Numbers are placed on the graph that correspond to the times shown in the snapshots of Fig. 4.

More dramatic synchronization is demonstrated in Fig. 6. Here the two cilia are initialized in opposite states; the cilium on the right begins in the recovery stroke, and the cilium on the left begins in the effective stroke. The velocity field in the second frame shows that at this stage, the cilia are indeed moving in opposite directions. The ciliary beats do synchronize and also settle into a regular beat frequency of about 64 Hz. The snapshots are not equally spaced in time, but show positions during the first couple of beat periods, and later positions during the fifth beat period. Fig. 7 shows the evolution of synchrony measured as described above. The simulations presented in Fig. 4 and Fig. 6 were performed with identical geometric, fluid, and numerical parameters—the only difference is the initial phase of the two cilia. In order to compare their course of synchronization, Fig. 8 shows each of their synchronization functions plotted on the same graph. We see that it takes longer for the two cilia started in opposite phases to synchronize, but after about $T = 0.05$ seconds, the beats are basically the same, slightly translated in time.

Fig. 9 shows snapshots of another simulation where the bases of three cilia are placed 1.5 cilium lengths apart; considerably further apart than the simulation above. Their configurations and dynein activation states are initially set at random phases within a recovery stroke. Synchrony again develops, but this time there is a marked phase difference between the three cilia. Periodic boundary conditions imposed in the horizontal direction of the fluid domain allow us to interpret these simulations as those of an infinite, linear array of cilia. Although periodic boundary conditions are imposed on the entire fluid domain, the cilia do not feel the presence of their periodic copies in the vertical direction because of the presence of the cell body wall. In essence, we are representing a linear array of cilia beating in a channel. Fig. 10 shows a sequence of overlays within a recovery stroke and a power stroke.

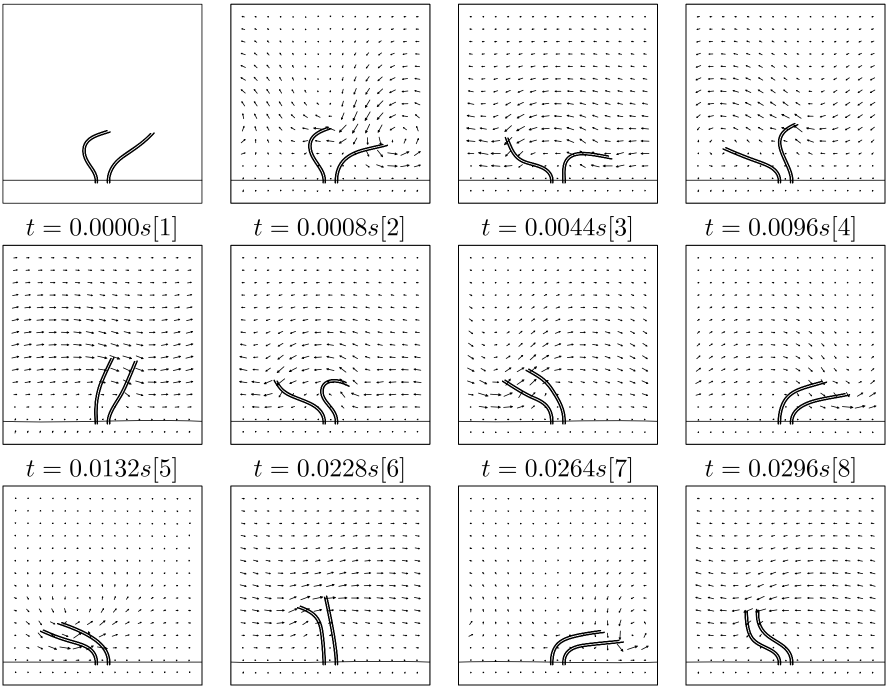

$t = 0.0000s[1]$ $t = 0.0008s[2]$ $t = 0.0044s[3]$ $t = 0.0096s[4]$

$t = 0.0132s[5]$ $t = 0.0228s[6]$ $t = 0.0264s[7]$ $t = 0.0296s[8]$

$t = 0.0732s[9]$ $t = 0.0752s[10]$ $t = 0.0788s[11]$ $t = 0.0868s[12]$

Fig. 6 Snapshots of synchronization of two cilia. The cilium on the left is initialized in its recovery stroke, and the cilium on the right is initialized in its effective stroke. The numbers in the bracket correspond to the denoted times on the synchronization graph shown in Fig. 7.

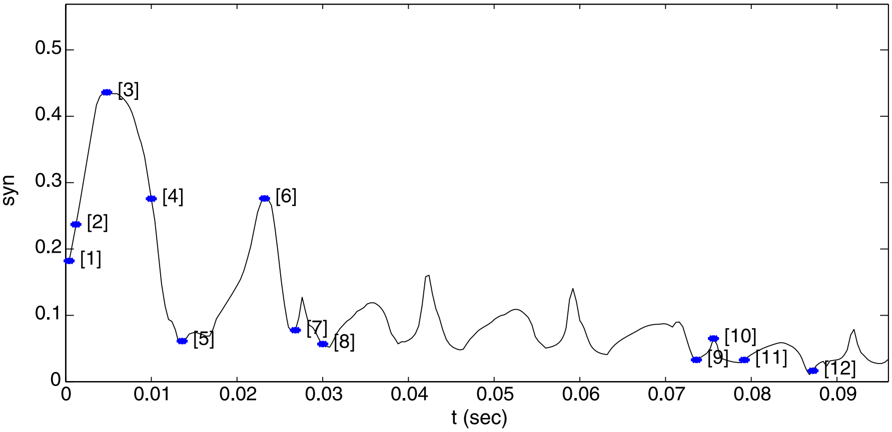

Fig. 7 Synchronization measurement for the simulation depicted in Fig. 6. The numbers shown on the graph correspond to the geometry of the two cilia shown in the indicated frame in Fig. 6.

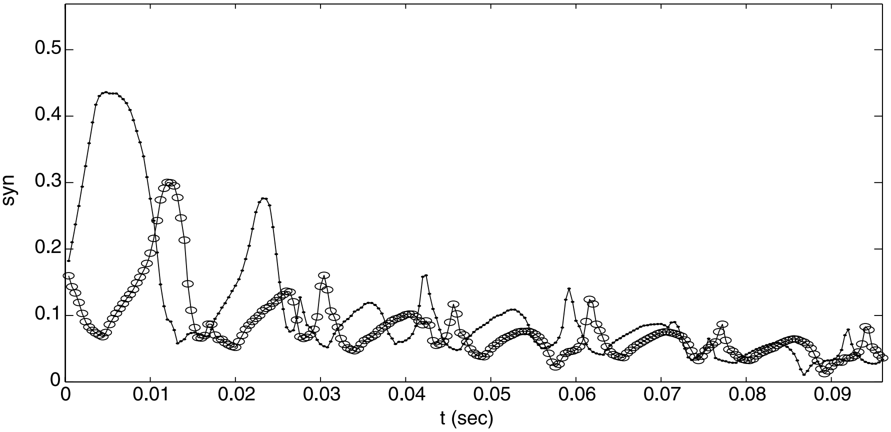

Fig. 8 The synchronization functions shown in Fig. 5 (curve marked with circles) and Fig. 7 (curve marked with dots) plotted together. Note that the two simulations eventually settle into a similar beat pattern.

Table 1 Frequency and flow rate for 1, 2, and 3 cilia

	Freq (Hz)	Flow rate (cm^2/s)	Net flow/beat (cm^2/beat)	Net flow/beat per cilium
1 cilium	48.48	257.64	5.31	5.31
2 cilia	60.60	409.76	6.76	3.38
3 cilia	61.67	494.93	8.04	2.68

3.2. Influence of neighboring cilia on beat frequency and flow rate

Gueron et al. (1997) reported that the beat frequency of their model cilium increases in the presence of neighboring cilia. To examine this feature, we performed simulations of 1, 2, and 3 cilia, each initialized with the same geometry and dynein activation states. Here the fluid domain is taken to be 80 µm × 40 µm, and the interciliary spacing is 2.4609 µm. The fluid domain is discretized using a 512 × 256 finite difference grid. Fig. 11 shows snapshots of each of these simulations at selected times. Subtle differences are noted in the beat geometries. There is a 25% increase in beat frequency as we move from one to two cilia, but less than 2% increase as we moved from two to three cilia (see Table 1). In the model cilia of Gueron et al. (1997), the beat frequency did not change significantly once the cilia number exceeded 10.

During the course of our simulation, the fluid velocity field is readily available at grid points of our underlying finite difference grid in the entire domain. We can monitor the total flow in the direction of beating from time $T = 0$ to $T = t$ by computing the integral:

$$Q(t) = \int_0^t \int_{\text{bottom}}^{\text{top}} u \, dy \, dt \tag{10}$$

where u is the x-component of the velocity field, and the integration is over any fixed vertical line. $Q(t)$ has units of cm^2. Note that due to incompressibility, this integral should

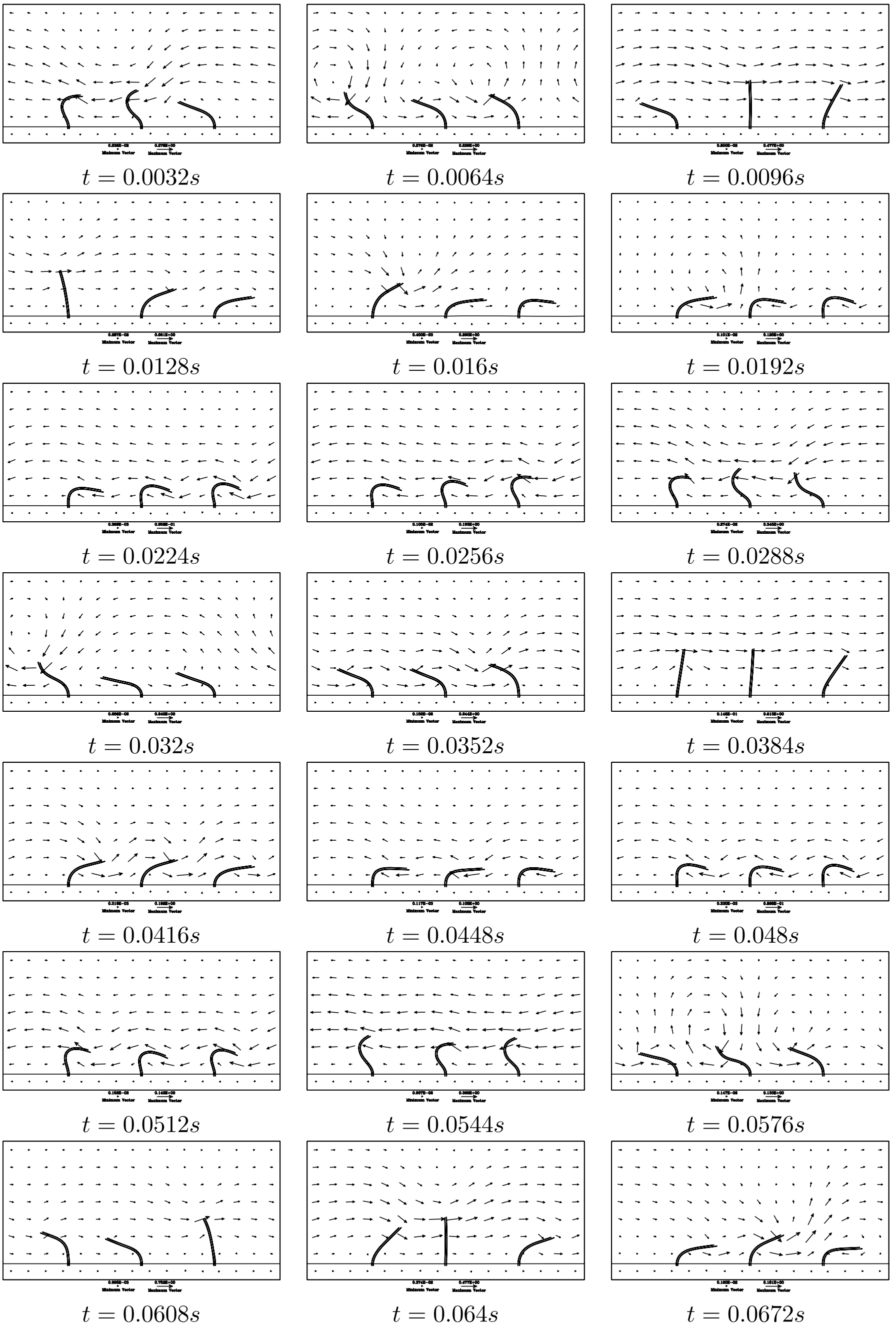
$t = 0.0032s$ $t = 0.0064s$ $t = 0.0096s$

$t = 0.0128s$ $t = 0.016s$ $t = 0.0192s$

$t = 0.0224s$ $t = 0.0256s$ $t = 0.0288s$

$t = 0.032s$ $t = 0.0352s$ $t = 0.0384s$

$t = 0.0416s$ $t = 0.0448s$ $t = 0.048s$

$t = 0.0512s$ $t = 0.0544s$ $t = 0.0576s$

$t = 0.0608s$ $t = 0.064s$ $t = 0.0672s$

Fig. 9 A ciliary array shows spontaneous metachrony. Snapshots of cilia geometry and velocity fields shown at equally spaced times.

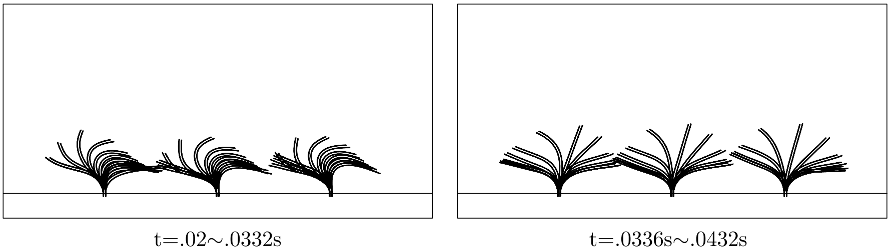

Fig. 10 Overlay of cilia geometry during recovery stroke (from time $t = 0.02$ to $t = 0.0332$ s) and in power stroke (from time $t = 0.0336$ s to $t = 0.0432$ s). Cilia positions are plotted at time intervals of 0.0012 s.

be the same at any cross section of the domain. Fig. 12 shows a plot of the total flow $Q(t)$ for each of the three simulations. During the power stroke, the flow in the positive x-direction increases, but there is substantial backflow during the recovery stroke. We remark that this backflow would be much less pronounced in a full three-dimensional ciliary beat when this return stroke is not in the plane of the recovery stroke. We may also compute the average flow rate over a period (the slope of the dashed lines in Fig. 12). This has units of cm^2/sec:

$$\hat{Q}(t) = \frac{1}{T_2 - T_1} \int_{T_1}^{T_2} \int_{\text{bottom}}^{\text{top}} u \, dy \, dt. \tag{11}$$

Here T_1 is the beginning of a power stroke and T_2 is the end of the subsequent recovery stroke. Although this average flow rate varies slightly from period to period, we take as the flow rate the average of this slope during the second and third period of beating. This flow rate is shown in Table 1. Here we see that the flow rate increased by 59% as we moved from one to two cilia and increased by more than 20% as we moved from two to three cilia. Thus, as we moved from two to three cilia, there was little change in beat frequency, but a significant change in flow rate. Note that that net flow per beat units of cm^2/beat for the ciliary array increases as the number of cilia increase (see Table 1). We can also examine how much each cilium is contributing to the fluid transport by looking at net flow per beat per cilium.

3.3. Effect of viscosity changes

In experimental investigations that measured beat frequency of paramecium cilia in fluids of different viscosities, Machemer reported that beat frequency decreased when viscosity increased (Machemer, 1972). Gueron et al. also reported this decrease in their model cilia (Gueron et al., 1997). Gheber et al. (1998) used double and triple simultaneous photoelectric measurements on cultured ciliary cells from the frog esophagus in the viscosity range of 1–2,000 cp and observed that increasing the viscosity of the medium caused not only a decrease in the ciliary beat frequency, but also changes in the metachrony and correlation between cilia.

We chose to examine the effect of viscosity on beat frequency and flow rate in simulations with two cilia as shown in Fig. 13 and Fig. 14. For the particular range of viscosities,

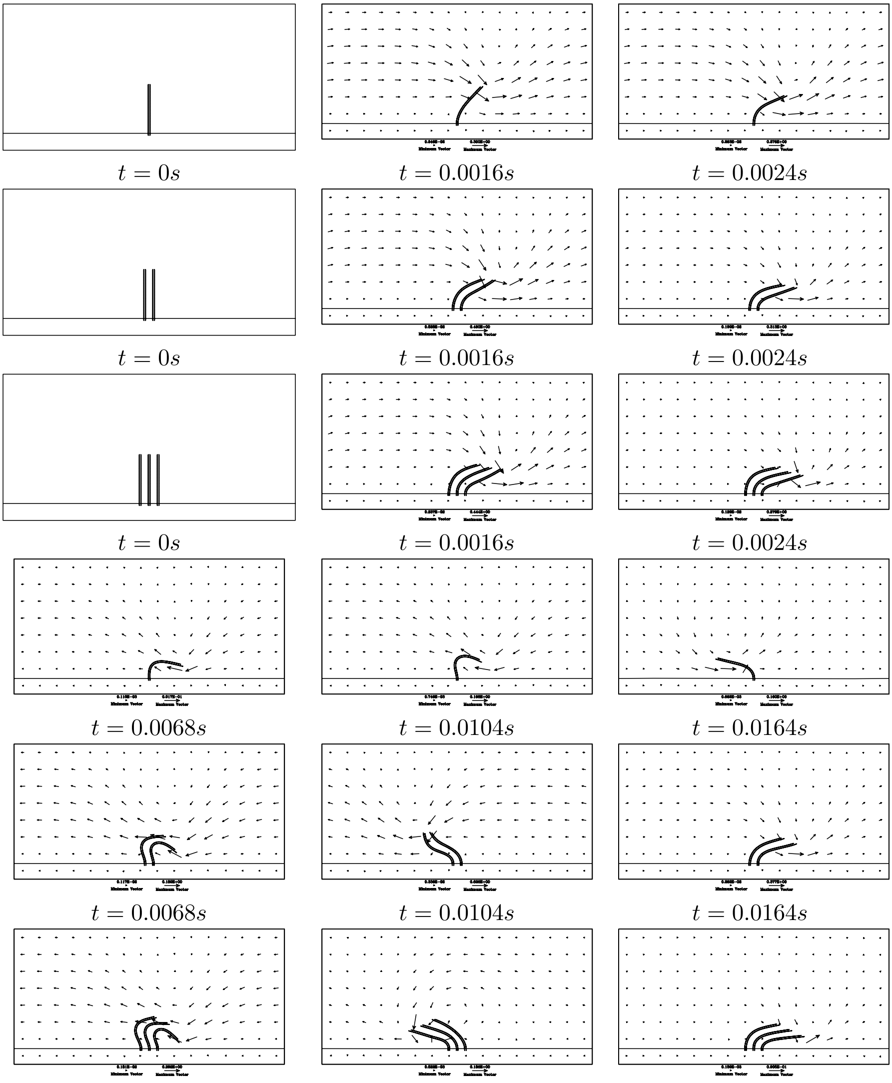
$t = 0s$ $t = 0.0016s$ $t = 0.0024s$

$t = 0s$ $t = 0.0016s$ $t = 0.0024s$

$t = 0s$ $t = 0.0016s$ $t = 0.0024s$

$t = 0.0068s$ $t = 0.0104s$ $t = 0.0164s$

$t = 0.0068s$ $t = 0.0104s$ $t = 0.0164s$

$t = 0.0068s$ $t = 0.0104s$ $t = 0.0164s$

Fig. 11 Comparison of the beats of 1, 2, and 3 cilia at selected times.

material parameters, and dynein-activation rules used in this model, the ciliary beats look virtually the same. Table 2 shows the computed beat frequencies, average flow rate, and net flow per beat as a function of viscosity. Following Machemer's presentation, Fig. 15 shows a plot of beat frequency versus the log of viscosity. Machemer (1972) argued that his measured data, plotted this way, exhibited a linear relationship. Fig. 15 also depicts the least squares linear fit to our computational results. As in the model cilia of Gueron et

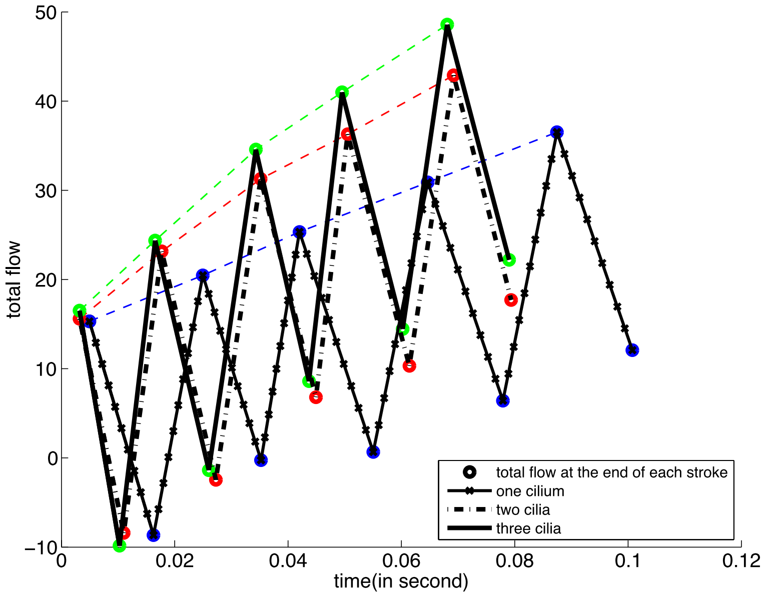

Fig. 12 Comparison of total flow pumped from left to right at the end of each stroke (power/recovery) for 1, 2, and 3 cilia with $\mu = 1.5$ cP.

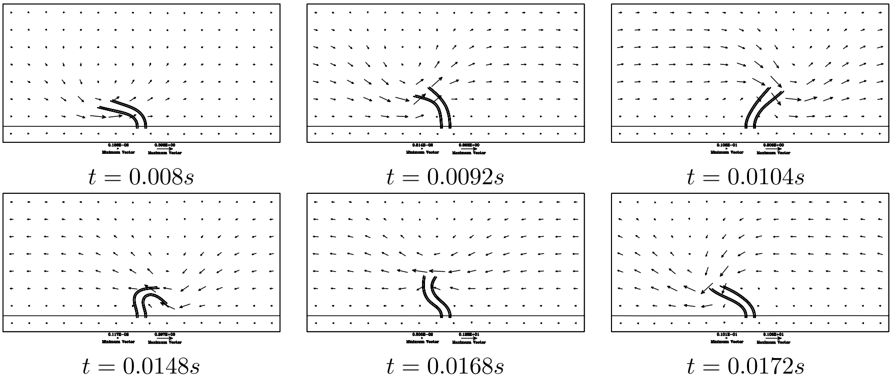
$t = 0.008s$ $t = 0.0092s$ $t = 0.0104s$

$t = 0.0148s$ $t = 0.0168s$ $t = 0.0172s$

Fig. 13 Snapshots of one complete beat (including a power stroke and a recovery stroke) from $t = 0.008$ s to $t = 0.0172$ s of 2 cilia with $\mu = 1.0$.

al. (1997), there is a deviation from linearity so that the frequency versus log of viscosity graph itself appears to be exponential.

As the viscosity decreases from 3.5 cP to 1.0 cP, the flow rate and frequency each increase approximately fourfold. However, from Table 2, we see that the net flow per beat is fairly constant for this range of viscosities, exhibiting only a 15% drop as viscosity is increased from 1 cP to 3.5 cP. This is not surprising since the geometry of the ciliary beats in these model cilia do not appear to change significantly with increased viscosity

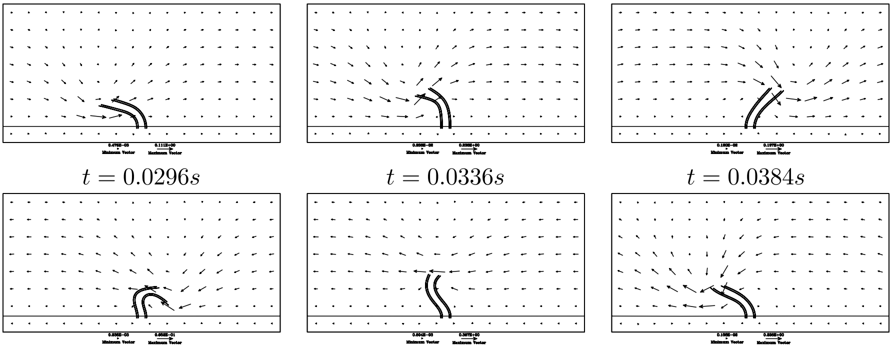

$t = 0.0296s$ $t = 0.0336s$ $t = 0.0384s$

$t = 0.0564s$ $t = 0.0644s$ $t = 0.0664s$

Fig. 14 Snapshots of one complete beat (including a power stroke and a recovery stroke) from $t = 0.0296$ s to $t = 0.0664$ s of 2 cilia with $\mu = 3.5$.

Table 2 Frequency of beat, flow rate, and net flow per beat with different viscosities

μ (cP)	Freq (Hz)	Flow rate	Net flow/beat
1.0	101.09	613.03	6.06
1.5	61.64	366.37	5.94
2.0	42.62	259.27	6.08
2.5	34.12	195.40	5.73
3.0	28.96	164.14	5.67
3.5	26.95	137.59	5.10

load. The change from 1 cP to 3.5 cP is quite modest compared with the viscosity range examined by Gheber et al. (1998). Related experiments examine flagellar waveforms of motile sperm placed in fluids of different viscosities. Note that eucaryotic sperm flagella are built out of the identical $9 + 2$ axonemal ultrastructure as cilia. Significant changes in emergent flagellar waveforms of sea-urchin sperm due to significant changes in external fluid viscosity have been reported (Tani and Kamimura, 1998). In addition, dramatic changes in the waveform of bull sperm have been shown to arise when the surrounding fluid was changed from Newtonian to non-Newtonian (Ho and Suarez, 2001).

3.4. *Effect of interciliary spacing*

Using particle imaging velocimetry, Solari et al. (2006) investigated the fluid motion around colonies of *Volvox carteri*. The fluid motion was induced by the cilium-like power and recovery strokes of the flagella that emanate from the spherical surface of the colony. These colonies are comprised of many flagellated cells along with germ cells. Growth of the colonies occurs as the germ cells grow, causing the distance between flagella on the surface of the colony to increase. Flow velocities near the surface of the colonies were measured during different growth phases. It was noted that the maximum fluid velocity was not monotonic as the distance between the flagella increased, but showed a peak at an intermediate stage. The measured beat frequencies and flagellar lengths at the different

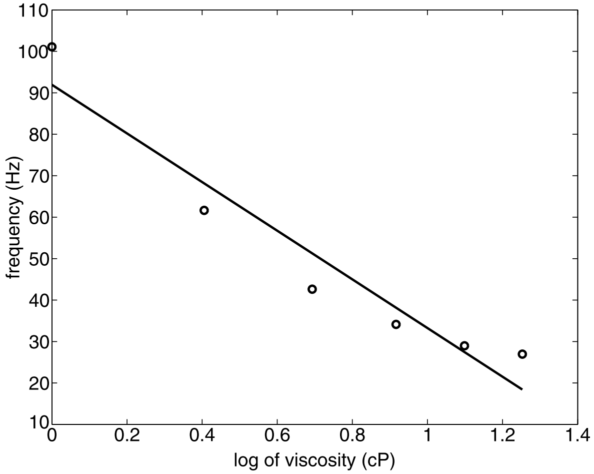

Fig. 15 Here we plot the measured beat frequency as a function of the log of viscosity along with the line that is the least squares fit of this data.

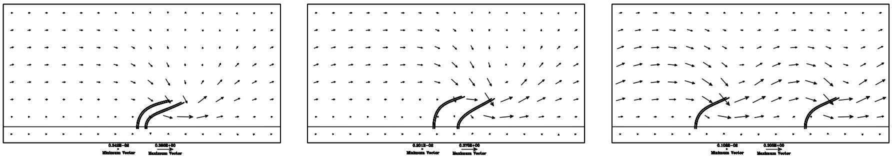

$d = .175$ $d = .5$ $d = 2.25$

Fig. 16 Three examples of two-cilia spacings. These show ciliary spacings of $d = 0.175, 0.5,$ and 2.25 ciliary lengths.

stages of colony growth did not show a dramatic change at the instance of peak velocity (Solari et al., 2006).

Motivated by these experiments, in this section we investigate how the spacing between two cilia affects their beat frequency and flow rate. We have already noted that there is a strong tendency for two cilia to synchronize when placed nearby. In order to minimize transient effects of synchronization, we place two identical model cilia in the fluid domain, initialized with identical dynein activation states. Our rectangular fluid domain has dimensions 80 µm × 40 µm. The cilia are 14 µm in length. Three examples of two-cilia spacings are depicted in Fig. 16. Note that we cannot space the cilia an arbitrary distance apart measured along the cell wall, since as they move apart, their periodic copies in the horizontal direction move closer.

Table 3 shows the measured beat frequency, flow rate, and net flow per beat in the two-cilia configurations for different spacings of their bases. Note that the net flow per beat is not a monotonic function of ciliary spacing, but shows a dramatic peak at a distance of one half of a cilium length (see Fig. 17). This is consistent with the observations of Solari et al. (2006).

Table 3 Emerging beat frequencies, flow rate, and net flow per beat in the two-cilia simulations as a function of the distance of their bases on the cell wall (measured in cilium lengths)

Distance in cilium lengths	Freq (Hz)	Flow rate	Net flow/beat
0.175	60.60	409.76	6.76
0.200	62.61	464.02	7.41
0.500	40.39	532.89	13.19
1.000	40.99	345.68	8.43
1.250	52.78	515.32	9.76
1.500	50.04	356.81	7.13
1.750	51.90	447.48	8.62
2.000	50.41	358.38	7.11
2.250	52.81	366.76	6.94

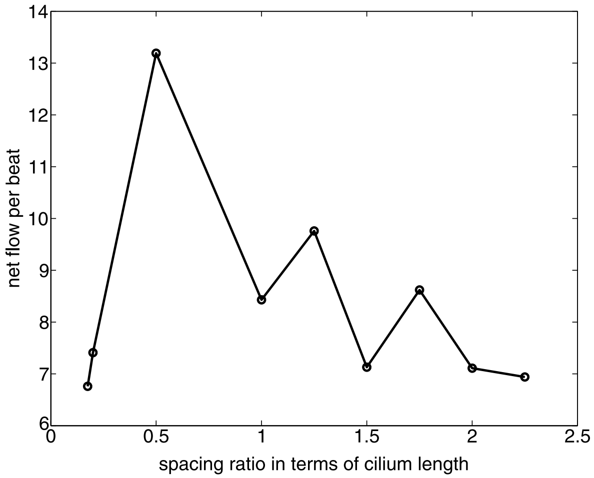

Fig. 17 Net flow per beat as a function of distance between the two cilia (measured in cilium lengths).

4. Discussion

The distinctive feature of this model is the detailed and biologically realistic mechanism by which the ciliary beat is produced. Unlike previous mathematical models, the ciliary beat form is not assumed and digitized data is not used to derive forces. The activation of the individual dyneins produces forces directly on the elastic structures of the ciliary axoneme. These forces generate the sliding between neighboring microtubule doublets that is converted into ciliary bending by the passive structures of the axoneme. It remains an open question as to just how it is that dyneins are uniformly activated or inactivated during the power stroke, and why there is a traveling wave of activation from base to tip during the recovery stroke. As this type of ciliary model is refined, one can consider the effect on the ciliary beat of defects in individual components within the axonemal structure and how these defects influence the global ciliary beating patterns.

Our model does predict the establishment of synchrony and metachrony due to hydrodynamic coupling of neighboring cilia. Our model shows that beat frequency decreases approximately linearly as a function of the logarithm of viscosity. This feature was also found experimentally by Machemer (1972) and in the model cilia of Gueron et al. (1997). We found that ciliary beat frequency increased dramatically as we increased from one to two cilia, and a much smaller increase in beat frequency as we added an additional cilium. The saturation in beat frequency was also noted in Gueron et al. (1997). Since our immersed boundary model gives us fluid velocities over the entire domain, we are able to easily calculate the flow rates and found that the flow rate per beat increased significantly as more cilia were added. Our study suggests that ciliary efficiency may depend critically on ciliary spacing. We found a significant peak in net flow per beat at an optimal ciliary spacing. This was also observed by Solari et al. (2006) in Volvox colonies.

While the actual coupled system consisting of the surrounding fluid and a ciliary array is obviously three-dimensional, the 2D results presented in this paper match the dynamics observed in experiment and other 3D models remarkably well. Moreover, this modeling framework can be used to test hypotheses concerning internal force generating mechanics of individual ciliary dyneins, such as Lindemann's geometric clutch hypothesis (Lindemann, 2007). Nevertheless, a fully 3D immersed boundary ciliary model is currently being developed.

Acknowledgements

The computational simulations were performed on the facilities of the Center for Computational Science, Tulane University, the Louisiana Optical Network Initiative (LONI), and the Mathematics Department of Washington State University. This work was supported by NSF DMS 0201063. The authors wish to thank Charlotte Omoto for her insight and many helpful discussions.

References

Afzelius, B.A., 1976. A human syndrome caused by immotile cilia. Science 193(4250), 317–319.

Afzelius, B.A., 2004. Cilia-related diseases. J. Pathol. 204, 470–477.

Avidor-Reiss, T., Maer, A.M., Koundakjian, E., Polyanovsky, A., Keil, T., Subramaniam, S., Zuker, C.S., 2004. Decoding cilia function: Defining specialized genes required for compartmentalized cilia biogenesis. Cell 117, 527–539.

Brokaw, C., 2001. Simulating the effects of fluid viscosity on the behaviour of sperm flagella. Math. Methods Appl. Sci. 24, 1351.

Brokaw, C., Luck, D., 1983. Bending patterns of chlamydomonas flagella i. Wild-type bending patterns. Cell Motil. 3, 131–150.

Brokaw, C.J., 1972. Flagellar movement: A sliding filament model. Science 178, 455–462.

Camalet, S., Jülicher, F., 2000. Generic aspects of axonemal beating. New J. Phys. 2, 24.1–24.23.

Childress, S., 1981. Mechanics of Swimming and Flying. Cambridge University Press, Cambridge.

Chilvers, M., O'Callaghan, C., 2000. Analysis of ciliary beat pattern and beat frequency using digital high speed imaging: Comparison with the photomultiplier and photodiode methods. Thorax 55, 314–317.

Darnton, N., Turner, L., Breuer, K., Berg, H., 2004. Moving fluid with bacterial carpets. Biophys. J. 86, 1863–1870.

Davenport, J.R., Yoder, B.K., 2005. An incredible decade for the primary cilium: A look at a once-forgotten organelle. Am. J. Physiol. Renal. Physiol. 289, F1159–F1169.

Dillon, R.H., Fauci, L.J., 2000. An integrative model of internal axoneme mechanics and external fluid dynamics in ciliary beating. J. Theor. Biol. 207, 415–430.

Dillon, R.H., Fauci, L.J., Omoto, C., 2003. Mathematical modeling of axoneme mechanics and fluid dynamics in ciliary and sperm motility. Dyn. Contin. Discrete Impuls. Syst. Ser. A Math. Anal. 10(5), 745–757. Progress in Partial Differential Equations (Pullman, WA, 2002).

Dresdner, R., Katz, D., Berger, S., 1980. The propulsion by large amplitude waves of uniflagellar microorganisms of finite length. J. Fluid Mech. 97, 591.

Eley, L., Yates, L.M., Goodship, J.A., 2005. Cilia and disease. Cur. Opin. Genet. Devel. 15, 308–314.

Fauci, L., McDonald, A., 1994. Sperm motility in the presence of boundaries. Bull. Math. Biol. 57, 679.

Fauci, L.J., Dillon, R.H., 2006. Biofluidmechanics of reproduction. Annu. Rev. Fluid Mech. 38, 371–394.

Fliegauf, M., Omran, H., 2006. Novel tools to unravel molecular mechanisms in cilia-related disorders. Trends Genet. 22(5), 241–245.

Flores, H., Lobaton, E., Mendez-Diez, S., Tlupova, S., Cortez, R., 2005. A study of bacterial flagellar bundling. Bull. Math. Biol. 67, 137–168.

Gheber, L., Korngreen, A., Priel, Z., 1998. Effect of viscosity on metachrony in mucus propelling cilia. Cell Motil. Cytoskel. 39(1), 9–20.

Gheber, L., Priel, Z., 1989. Synchronization between beating cilia. Biophys. J. 55, 183–191.

Gray, J., 1928. Ciliary Movement. Cambridge University Press, Cambridge.

Gray, J., Hancock, G., 1955. The propulsion of sea-urchin spermatoza. J. Exp. Biol. 32, 802–814.

Gueron, S., Levit-Gurevich, K., 1998. Computation of the internal forces in cilia: Application to ciliary motion, the effects of viscosity, and cilia interactions. Biophys. J. 74(4), 1658–1676.

Gueron, S., Levit-Gurevich, K., 1999. Energetic considerations of ciliary beating and the advantage of metachronal coordination. Proc. Natl. Acad. Sci. USA 96(22), 12240–12245.

Gueron, S., Levit-Gurevich, K., 2001. A three-dimensional model for ciliary motion based on the internal $9 + 2$ structure. Proc. Biol. Sci. 268(1467), 599–607.

Gueron, S., Levit-Gurevich, K., Liron, N., Blum, J.J., 1997. Cilia internal mechanism and metachronal coordination as the result of hydrodynamical coupling. Proc. Natl. Acad. Sci. USA 94(12), 6001–6006.

Guirao, B., Joanny, J.-F., 2007. Spontaneous creation of macroscopic flow and metachronal waves in an array of cilia. Biophys. J. 92, 1900–1917.

Higdon, J., 1979a. A hydrodynamic analysis of flagellar propulsion. J. Fluid Mech. 90, 685.

Higdon, J., 1979b. The hydrodynamics analysis of flagellar propulsion: Helical waves. J. Fluid Mech. 94, 331.

Hines, M., Blum, J., 1978. Bend propagation in flagella i. Derivation of equations of motion and their simulation. Biophys. J. 23, 41.

Hines, M., Blum, J., 1979. Bend propagation in flagella ii. Incorporating of dynein cross-bridge kinetics into the equations of motion. Biophys. J. 25, 421.

Ho, H., Suarez, S., 2001. Hyperactivation of mammalian spermatozoa: Function and regulation. Reproduction 122, 519.

Howard, J., 2001. Mechanics of Motor Proteins and the Cytoskeleton. Sinauer Assoc., Sunderland.

Ishijima, S., Hiramoto, Y., 1994. Flexural rigidity of echinoderm sperm flagella. Cell Struct. Funct. 19(6), 349–362.

Kim, M., Bird, J., Van Parys, J., Breuer, K., Powers, T., 2003. A macroscopic scale model of bacterial flagellar bundling. Proc. Natl. Acad. Sci. USA 100(26), 15481–15485.

Lighthill, J.L., 1967. Flagellar hydrodynamics. SIAM Rev. 18, 161–230.

Lim, S., Peskin, C., 2004. Simulations of the whirling instability by the immersed boundary method. SIAM J. Sci. Comput. 25(6), 2066–2083.

Lindemann, C., 2003. Structural-functional relationships of the dynein, spokes, and central-pair projections predicted from an analysis of the foces acting within a flagellum. Biophys. J. 84, 4115–4126.

Lindemann, C., 2007. The geometric clutch as a working hypothesis for future research on cilia and flagella. Ann. N.Y. Acad. Sci. 1101, 477–493.

Machemer, H., 1972. Ciliary activity and the origin of metachrony in paramecium: Effects of increased viscosity. J. Exp. Biol. 57(1), 239–259.

Marshall, W.F., Nonaka, S., 2006. Cilia: Tuning in to the cell's antenna. Curr. Biol. 16(15), R604–R614.

Mitchell, B., Jacobs, R., Li, J., Chien, S., Kintner, C., 2007. A positive feedback mechanism governs the polarity and motion of motile cilia. Nature 447, 97–101.

Murase, M., 1992. The Dynamics of Cellular Motility. Wiley, Chichester.

Pan, J., Wang, Q., Snell, W.J., 2005. Cilium-generated signaling and cilia-related disorders. Lab. Invest. 85, 452–463.

Peskin, C.S., 1977. Numerical analysis of blood flow in the heart. J. Comput. Phys. 25(3), 220–252.

Peskin, C.S., 2002. The immersed boundary method. Acta Numer. 11, 479–517.

Phan-Thien, N., Tran-Cong, T., Ramia, M., 1987. A boundary element analysis of flagellar propulsion. J. Fluid Mech. 184, 533.

Powers, T., 2001. Role of body rotation in bacterial flagellar bundling. Phys. Rev. E 65, 040903.

Snell, W.J., Pan, J., Wang, Q., 2004. Cilia and flagella revealed: From flagellar assembly in chlamydomonas to human obesity disorders. Cell 117, 693–697.

Solari, C.A., Ganguly, S., Kessler, J.O., Michod, R.E., Goldstein, R.E., 2006. Multicellularity and the functional interdependence of motility and molecular transport. Proc. Natl. Acad. Sci. USA 103, 1353–1358.

Talbot, P., Geiske, C., Knoll, M., 1999. Oocyte pickup by the mammalian oviduct. Mol. Biol. Cell 10(1), 5–8.

Tani, T., Kamimura, S., 1998. Reactivation of sea-urchin sperm flagella induced by rapid photolysis of caged atp. J. Exp. Biol. 201, 1493–1503.

Taylor, G., 1951. Analysis of the swimming of microscopic organisms. Proc. R. Soc. 209, 447.

Vilfan, A., Jülicher, F., 2006. Hydrodynamic flow patterns and synchronization of beating cilia. Phys. Rev. Lett. 96, 058102.

Vogel, G., 2005. Betting on cilia. Science 310(5746), 216–218.

Wiggins, C.H., Goldstein, R.E., 1998. Flexive and propulsive dynamics of elastica at low Reynolds number. Phys. Rev. Lett. 80, 3879–3882.

Wiggins, C.H., Riveline, D., Ott, A., Goldstein, R.E., 1998. Trapping and wiggling: Elastohydrodynamics of driven microfilaments. Biophys. J. 74(2), 1043–1060.

Witman, G., 1990. Introduction to cilia and flagella. In: R. Bloodgood (Ed.), Ciliary and Flagellar Membranes, p. 1. Plenum, New York.